JOURNAL OF AIRCRAFT
Vol. 46, No. 6, November–December 2009

Sonic Boom Variability Due to Homogeneous Atmospheric Turbulence

Hiroshi Yamashita* and Shigeru Obayashi†
Tohoku University, Sendai 980-8577, Japan

DOI: 10.2514/1.40215

This study describes the nondeterministic effect of homogeneous atmospheric turbulence on sonic boom propagation. The Sears–Haack body was calculated in three dimensions by computational fluid dynamics in inviscid flow (Euler) mode to create the near-field pressure wave. The homogeneous atmospheric turbulence field was represented by the finite sum of discrete Fourier modes based on the von Karman and Pao energy spectrum. The sonic boom signature was then calculated by the modified waveform parameter method, considering a random velocity of homogeneous atmospheric turbulence. The results of this study indicated that atmospheric turbulence has a marked influence on sonic boom overpressure during its propagation to the ground. In comparison to the no-turbulence condition, we found that the sonic boom decreased in 59% of the cases and increased in 41% of the cases. Thus, homogeneous atmospheric turbulence seems to favor a decrease, rather than an increase, in boom overpressure. In addition, we found that turbulence has a small effect on the propagation path from the flight altitude to the ground. Nonetheless, this small change in the propagation path may result in a variability, of the point at which the sonic boom reaches the ground, of up to 1820 ft in the north–south direction (flight direction) and 115 ft in the east–west direction.

Nomenclature

AL	=	body reference length in feet
a	=	speed of sound
E	=	von Karman and Pao energy spectrum
F	=	coefficient for unit normal vector calculation
H	=	flight altitude above the ground in feet
h	=	distance taken perpendicularly from the body chord axis to the ground direction
K	=	turbulent kinetic energy
k	=	wave number
k_d	=	dissipation wave number of the energy spectrum
k_e	=	peak wave number of the energy spectrum
k_l	=	wave number corresponding to the largest eddy scale
$\boldsymbol{k_n}$	=	wave vector of the nth Fourier mode
l	=	longitudinal dimension and body reference length used by computational fluid dynamics
M	=	Mach number
ML	=	model reference length
N	=	number of Fourier components
$\boldsymbol{N}$	=	wave front unit normal vector
N_x, N_y	=	horizontal components of wave front unit normal vector
N_z	=	vertical component of wave front unit normal vector
P	=	pressure
$\boldsymbol{R}$	=	ray path vector
r	=	radius distribution
t	=	time
$\boldsymbol{u_t}$	=	turbulence velocity field
$\tilde{u}_{tn}$	=	amplitude of the nth Fourier mode
V	=	total volume
$\boldsymbol{V}$	=	wind velocity vector
V_{rms}	=	root mean square of turbulent velocity
V_x, V_y	=	horizontal components of the wind velocity vector
V_z	=	vertical components of the wind velocity vector
x, y, z	=	Cartesian coordinates
$\boldsymbol{y}$	=	given point of the turbulent velocity field
ΔP	=	overpressure
ε	=	turbulence dissipation rate
$\boldsymbol{\sigma_n}$	=	direction of the nth Fourier mode
Ψ_n	=	phase of the nth Fourier mode

Subscripts

n	=	Fourier mode
0	=	ambient
∞	=	freestream

Received 3 August 2008; revision received 30 June 2009; accepted for publication 10 August 2009.

*Graduate Student, Institute of Fluid Science, Student Member AIAA.
†Professor, Institute of Fluid Science, Associate Fellow AIAA.

I. Introduction

AT PRESENT, there are several technical problems that prevent the use of supersonic aircraft for commercial transport, including engine exhaust emissions, airport noise (especially during takeoff or landing), and sonic boom [1]. Particularly, sonic boom must be reduced significantly to make supersonic transport (SST) feasible [2,3]. Kusunose et al. [4–8] and Kuratani et al. [9] have examined the biplane concept to design a low boom configuration. This concept allows significant reduction of sonic boom using a Busemann-type biplane.

In supersonic biplane design, it is necessary to evaluate the influence of the sonic boom on the ground. Before reaching the ground, the sonic boom propagates through the real atmosphere, which is not a uniform field. Therefore, the sonic boom can be affected by atmospheric conditions, such as temperature gradient, wind distribution with height, atmospheric turbulence, etc. Previous experimental studies indicated that atmospheric variations could bring about distortions in the sonic boom propagation path and also in its pressure signature, leading to variations in the sonic boom overpressure [10–12]. To model these real conditions, it is necessary to develop a simulation code that accounts for the influence of a real atmospheric field.

Here, we present a method for sonic boom estimation that takes into consideration homogeneous atmospheric turbulence, including nondeterministic effects of atmospheric turbulence on sonic boom propagation. In particular, we focused on the variability of the initial overpressure, tail overpressure, and propagation path.

This paper is organized as follows. Section II presents a brief description of the numerical models and methods used for sonic boom calculation. Section III presents the results and discussion for 100 different randomly generated turbulent fields. Finally, Section IV concludes this study.

II. Numerical Models and Methods

Figure 1 shows the logical flowchart of the sonic boom calculation program used in this study. The computational procedure consisted of the following three components. First, the near flowfield was calculated using computational fluid dynamics (CFD) for a three-dimensional Euler flow, and the near-field pressure was then extracted from the CFD results. Second, a random velocity field of homogeneous atmospheric turbulence was calculated from the finite sum of discrete Fourier modes. Finally, the sonic boom signature on the ground was calculated by the modified waveform parameter method [13,14], using the near-field pressure wave and the homogeneous turbulent field as input data.

With regard to the homogeneous atmospheric turbulent field, we created 100 different turbulent fields by random number generation. The resulting 100 different sonic boom signatures were assessed with regard to the nondeterministic effects of atmospheric turbulence on sonic boom [15]. In addition, the turbulent field was assumed to be frozen (i.e., the turbulent velocity is constant during sonic boom propagation). This is reasonable, because sonic boom propagation occurs on a much smaller time scale than the evolution of turbulence structures [16,17]. The following sections describe the calculation methodology in detail.

A. Computational Fluid Dynamics Calculation of the Near Field

The flow around a Sears–Haack body was calculated in three dimensions using CFD [UPACS (Unified Platform for Aerospace Computational Simulation) code [18], developed at the Japan Aerospace Exploration Agency in Euler mode, mainly focusing on shock wave properties around the body. The angle of attack was set to zero at $M_\infty = 1.7$ for supersonic steady flight. The Sears–Haack body was investigated, because this configuration can create a simple N wave in a relatively short distance, thus making it easy to understand the effects of homogeneous atmospheric turbulence on sonic boom propagation. A delay of complicated waveform distortion due to nonlinearity, as in the case of a shaped sonic boom signature that can avoid coalescence of the N wave, is not related to this study. The definition of a Sears–Haack body is as expressed in [19,20]:

$$\frac{r}{r_{\max}} = \left[1 - \left(\frac{x}{l/2}\right)^2\right]^{3/4} \left(-\frac{l}{2} \le x \le \frac{l}{2}\right) \tag{1}$$

where $r_{\max}$ is the maximum radius and was set as $r_{\max} = 0.052$ with respect to the dimensionless body length $l = 1.0$. The total volume of the body became $V = 0.005$.

Figure 2 shows the structured grid of the Sears–Haack body used for the three-dimensional near-field calculation, in which the grid is aligned with a Mach number 1.7 shock to obtain a near-field high accuracy pressure distribution. We calculated only half of the body, due to its symmetry. The number of grid points on the surface of the body was 4,200, and the total number of grid points was approximately 3.0 million for the near-field calculation (from 0.0 to 8.0 body lengths).

With regard to the reliability of CFD analysis using the UPACS code, it was demonstrated previously [5] that the CFD results and analytical results derived from the supersonic thin airfoil theory [21] showed good agreement. Therefore, we were not concerned here with validation. A detailed description of the UPACS code has been reported elsewhere [18].

B. Generation of the Homogeneous Atmospheric Turbulent Field

A random velocity field of homogeneous atmospheric turbulence is created by first using the energy spectrum of von Karman and Pao [22], which is defined by

$$E(k) = \left(\frac{2}{3}\right)^{3/2} \frac{K^{5/2}}{\varepsilon} \frac{(k/k_e)^4}{[1 + (k/k_e)^2]^{17/6}} \exp\left[-\frac{9}{4}\left(\frac{k}{k_d}\right)^{4/3}\right] \tag{2}$$

where k is the wave number and k_e is the peak wave number of the energy spectrum. In addition, k_d is the dissipation wave number of the spectrum. In the field of meteorology, atmospheric phenomena are classified according to their time and space scales [23], such that we have microscale phenomena (such as turbulence in an atmospheric boundary layer), mesoscale phenomena [which include cumulonimbus clouds (thunderhead) and hurricanes], and macroscale phenomena (such as the monsoons). In the present model, we used the microscale fluctuations defined by this classification to generate a homogeneous atmospheric turbulent field. From this, the parameters were given as follows: $k_e = 6.28 \times 10^{-3}$ m^{-1} and $k_d = 628$ m^{-1}, and the wave number corresponding to the largest eddy was set as $k_l = 3.14 \times 10^{-3}$ m^{-1} (as described previously [24]). In addition, the parameters K and ε were estimated using experimental data reported elsewhere [25–27]; the kinetic energy of turbulence was estimated as $K = 0.4$ m^{2}s^{-2} and the turbulence dissipation rate as $\varepsilon = 1.15 \times 10^{-4}$ m^{2}s^{-3} in this study.

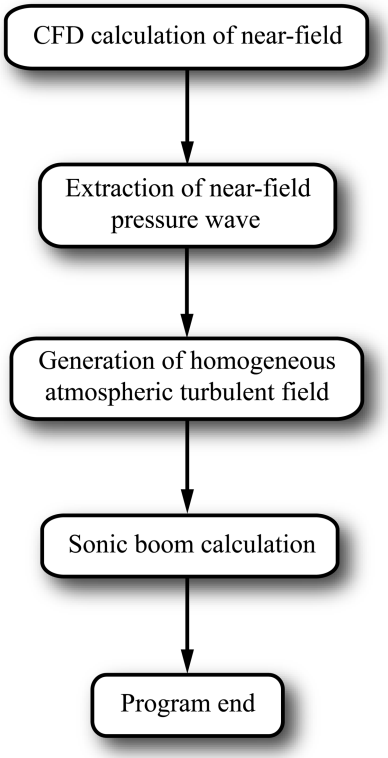

Fig. 1 Logical flow chart of the sonic boom calculation program.

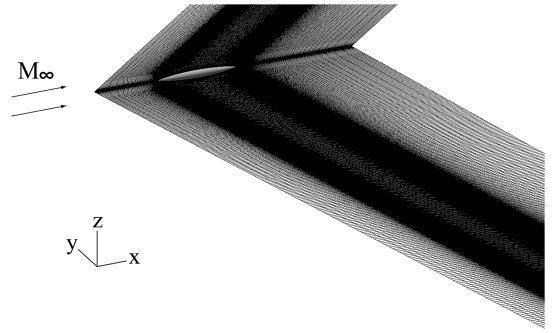

Fig. 2 Structured grid of the Sears–Haack body in a symmetry plane, used for CFD (UPACS code) analysis. The grid is aligned with the shock waves generated at Mach number $M_\infty = 1.7$.

After the energy spectrum was defined, the random turbulent velocity field was generated using a finite sum of N discrete Fourier modes, as defined in Eq. (3). The method has been used in previous studies to create a turbulent velocity field [24,28]. Therefore, we used $N = 200$ Fourier modes in all calculations:

$$\boldsymbol{u}_t(\boldsymbol{y}) = 2\sum_{n=1}^{N} \tilde{u}_{tn} \cos(\boldsymbol{k}_n \cdot \boldsymbol{y} + \Psi_n)\boldsymbol{\sigma}_n \tag{3}$$

where $\boldsymbol{y}$ is a given point of the turbulent velocity field.

The grid width of the turbulent field was $2 \times 15 \times 18.5$ km in the x, y, and z directions, respectively. The total number of grid points was approximately 600,000 for the whole field, and the grid spacing was 100 m in all directions. Turbulent velocities with microscale fluctuations were randomly assigned throughout the turbulent field. Figure 3 confirms that all 100 randomly generated turbulent fields had rms velocities very close to $V_{\text{rms}} = 2.5$ ms^{-1} using the parameters listed after Eq. (2).

C. Sonic Boom Calculation

Sonic boom was calculated by the modified waveform parameter method [13,14]. This method is based on geometric acoustics and isentropic wave theory, and it allows the calculation of wave amplitude, nonlinear waveform distortion, and ray tracing. Figure 4 shows a ray path (solid line) through a homogeneous atmospheric turbulent field. In this model, the grid points of the turbulent field do not coincide with the ray tracing calculation points. Therefore, a trilinear interpolation was performed on the random turbulent velocities into the ray path, as shown in Fig. 5. The ray tracing can be determined from the following set of equations (4) and (5):

$$\boldsymbol{R}(I+1) = \boldsymbol{R}(I) + \Delta\boldsymbol{R}(I) \tag{4}$$

$$\boldsymbol{N}(I+1) = \boldsymbol{N}(I) + \Delta\boldsymbol{N}(I) \tag{5}$$

where $\boldsymbol{R}(I)$ is a ray path vector and $\boldsymbol{N}(I)$ is a wave front unit normal vector. The increments $\Delta\boldsymbol{R}(I)$ and $\Delta\boldsymbol{N}(I)$ are given by Eqs. (6–8):

$$\Delta\boldsymbol{R}(I) = [a_0(I)\boldsymbol{N}(I) + \boldsymbol{V_0}(I)]\Delta t \tag{6}$$

$$\Delta\boldsymbol{N}(I) = \begin{bmatrix} \Delta N_x(I) \\ \Delta N_y(I) \\ \Delta N_z(I) \end{bmatrix} = F(I) \begin{bmatrix} N_x(I)N_z(I) \\ N_y(I)N_z(I) \\ -N_x^2(I) - N_y^2(I) \end{bmatrix} \Delta t \tag{7}$$

$$F(I) = N_x(I)\frac{\mathrm{d}V_{0x}}{\mathrm{d}z}(I) + N_y(I)\frac{\mathrm{d}V_{0y}}{\mathrm{d}z}(I) + N_z(I)\frac{\mathrm{d}V_{0z}}{\mathrm{d}z}(I) + \frac{\mathrm{d}a_0}{\mathrm{d}z}(I) \tag{8}$$

where Δt is the time increment between the Ith and $(I+1)$th calculation points. The path integral calculation was performed by a fourth-order Runge–Kutta method, and the vertical component of turbulent velocity V_z was included for ray tracing. We assumed a quasi-stratified atmosphere [29], as the atmospheric turbulent velocity is much smaller than the local speed of sound in the atmosphere. In fact, the rms velocity of homogeneous atmospheric turbulence was set as $V_{\text{rms}} = 2.5$ ms^{-1}, whereas the local speed of sound is around $a_0 = 300$ ms^{-1}.

The initial conditions for the waveform parameter method were set as follows: the flight Mach number $M_\infty = 1.7$, the flight altitude above ground $H = 60,000$ ft (around 18.3 km), the model reference length $ML = 1.0$, and the body reference length $AL = 202$ ft (total length of the Concorde aircraft). The temperature gradient of the standard atmosphere [30] was used, as we were concerned here only with the effects of homogeneous atmospheric turbulence on the sonic boom, and the effects of temperature distributions in the atmosphere were not considered in this study. In addition, sonic boom signatures were calculated from the flight altitude to the ground using only the rays that were initially emitted in the vertical plane, as shown in Fig. 4, because the propagation distance becomes shortest in this plane, and the strongest sonic boom overpressure is measured in this plane for the axisymmetric Sears–Haack body.

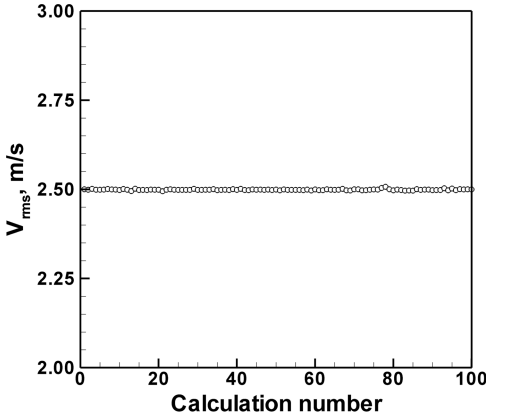

Fig. 3 V_{rms} values of 100 different randomly generated fields, calculated using a homogeneous atmospheric turbulence model.

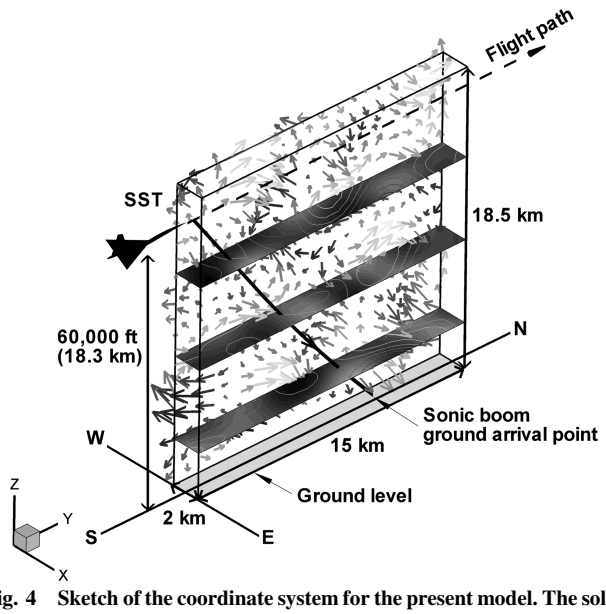

Fig. 4 Sketch of the coordinate system for the present model. The solid line shows a ray path of the sonic boom through a homogeneous atmospheric turbulent field, propagating from the flight altitude to the ground.

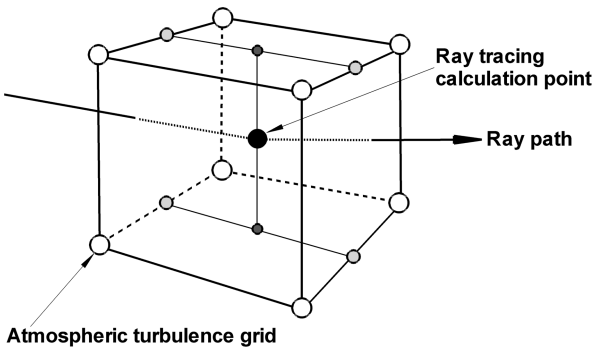

Fig. 5 Trilinear interpolation of random atmospheric turbulence velocity for the ray path calculation.

III. Results and Discussion

A. Determination of the Near-Field Pressure Wave for Sonic Boom Calculation

To determine the near-field pressure wave to be used as input data for the sonic boom propagation calculation, the comparison of near-field pressure signatures for the Sears–Haack body at $h/l =$ 1.0–5.0 are plotted in Fig. 6. In addition, Fig. 7 shows the sonic boom signatures calculated without atmospheric turbulence using the near-field pressure signatures at $h/l = 1.0$–5.0. This is shown because the accuracy of sonic boom calculation is dependent on confirmation of the grid dependency and the three-dimensional effect of the flow [31]. As shown Fig. 7, the sonic boom ground signature was the same, regardless of the starting point. That is, the grid quality was adequate for capturing a near-field pressure wave with sufficient accuracy. Therefore, in this study, the near-field pressure signature at $h/l = 5.0$ was used as input data for the sonic boom calculation.

B. Variability of Sonic Boom Overpressure

Figure 8a shows the calculated sonic boom signatures for the no-turbulence case, whereas Fig. 8b shows the 100 different signatures calculated with 100 different turbulent fields. These results confirmed that there is variability in the sonic boom signature due to homogeneous atmospheric turbulence, although all sonic boom waves were calculated using the same near-field pressure wave extracted at $h/l = 5.0$ (as shown in Fig. 6).

With regard to the variability of sonic boom overpressure, the initial and tail overpressure for the no-turbulence case were $\Delta P =$ 1.09 psf and $\Delta P = -1.15$ psf, respectively. In the turbulence cases,

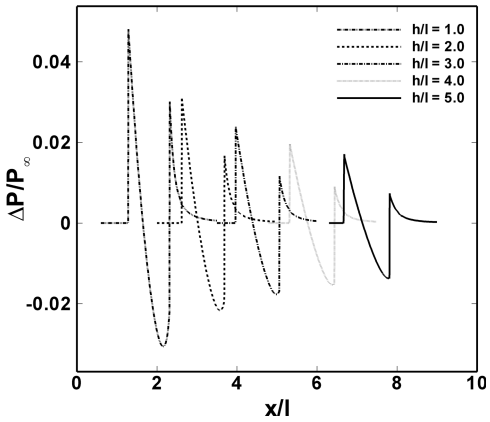

Fig. 6 Comparison of near-field pressure signatures propagating from the Sears–Haack body at $h/l = 1.0$–5.0.

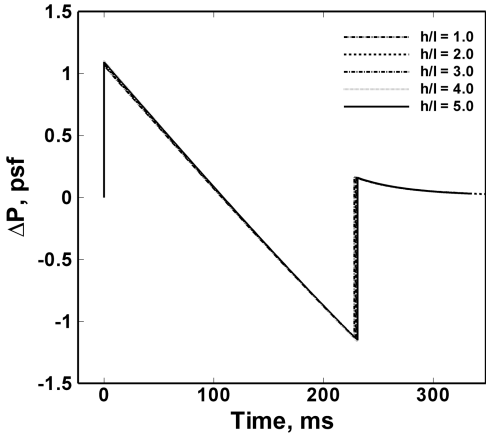

Fig. 7 Comparison of sonic boom signatures on the ground, calculated from five different near-field pressure waves without homogeneous atmospheric turbulence: the flight Mach number $M_\infty = 1.7$, the flight altitude $H = 60,000$ ft, the model reference length $ML = 1.0$, and the body reference length $AL = 202$ ft.

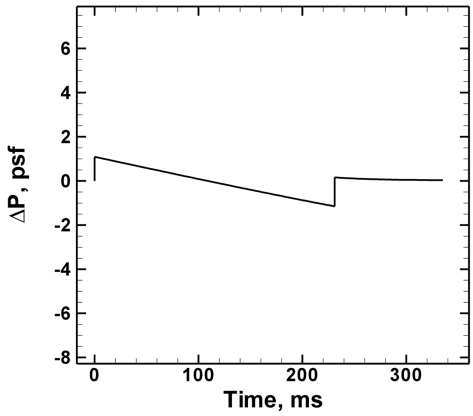

a) No-turbulence

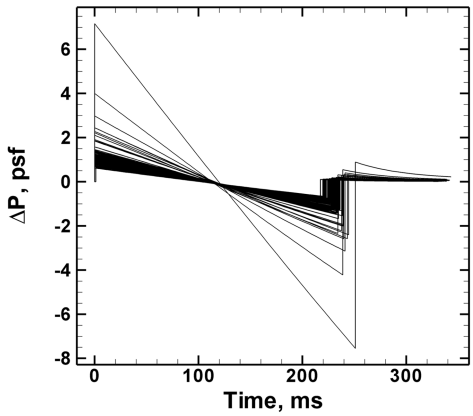

b) Turbulence

Fig. 8 Calculated sonic boom signatures for all cases: a) no-turbulence case and b) turbulence cases, including 100 different signatures.

on the other hand, the initial and tail overpressures were distributed over a wide range. The initial overpressure ranged from $\Delta P = 0.62$ to $\Delta P = 7.17$ psf, whereas the tail overpressure ranged from $\Delta P = -0.65$ to $\Delta P = -7.55$ psf. In addition, a strong correlation was confirmed between both overpressures in Fig. 8b (i.e., cases with high initial overpressure also had strong tail overpressure). This was because the present model focuses on variability of sonic boom overpressures due to atmospheric turbulence. The turbulence affects the ray tracing calculation and varies the ray tube area, which results in variation of both overpressures. A model that accounts for turbulent distortion of sonic boom signature was not included.

The influence of the homogeneous atmospheric turbulence on the sonic boom signature loudness metric was confirmed for reference, although the present model accounts only for the variations in overpressure. We calculated the A-weighted sound exposure level (ASEL) on the following three signatures: the no-turbulence case, the turbulence case with maximum overpressure, and the turbulence case with minimum overpressure. To estimate the rise time of the respective sonic boom signatures, we employed the rise time prediction model [31,32], based on the three series, the molecular absorption theory, the empirical model, and the outer boundary of the flyover data; each series represents the rise time as a function of shock overpressure ΔP. For the rise time calculation for three signatures, we added the estimated rise time to the respective sonic boom signatures on the ground by assuming the straight line approximation from the onset of shock to shock maximum and shock minimum to the end of the shock. Table 1 shows the resulting ASEL values for the three cases. As indicated in Table 1, there was a wide degree of variation in loudness value, due to atmospheric turbulence in all series. However, it is important to note that this variation in the loudness metric was a narrow result obtained using the present model under specific conditions (e.g., the atmospheric turbulence was generated throughout the whole space, as shown in Fig. 4).

Table 1 Calculated ASEL of sonic boom signatures for the following three cases: the no-turbulence case and cases with maximum and minimum overpressures among the 100 cases calculated with homogeneous atmospheric turbulence

Case	Series		
	Molecular absorption theory	Empirical model	Outer boundary of flyover data
No-turbulence, dBA	84.4	78.5	72.8
Turbulence with max ΔP, dBA	107.7	105.2	103.7
Turbulence with min ΔP, dBA	75.9	69.1	62.6

Figure 9 shows the frequency distributions of relative initial and tail overpressures in the presence of atmospheric turbulence, with a bin size of 0.25 in both Figs. 9a and 9b. The horizontal axes show the $\Delta P_{\text{Turbulence}}/\Delta P_{\text{No-turbulence}}$ ratio, where $\Delta P_{\text{Turbulence}}$ is the overpressure for each of the 100 cases with atmospheric turbulence and $\Delta P_{\text{No-turbulence}}$ is the value of overpressure for the no-turbulence case (as shown in Fig. 8a). Figure 9 shows that under turbulent conditions, sonic boom overpressure may decrease by as much as half when compared with the value of the no-turbulence case, but it may also increase to more than double this value. This variability was compared with past actual ground-based measurements taken for an XB-70 aircraft (June 1966) of about 185 ft in length [11,33,34]. The ratio of $\Delta P_{\text{MEAS}}/\Delta P_{\text{CALC}}$ in Fig. 10a corresponds to the ratio of $\Delta P_{\text{Turbulence}}/\Delta P_{\text{No-turbulence}}$ in Fig. 10b, because ΔP_{MEAS} is the measured overpressure value taken during a test flight and thus includes the atmospheric turbulence effect in the real atmosphere; whereas, ΔP_{CALC} is the predicted value calculated for a nonturbulent stratified atmosphere under standard atmospheric conditions. The variability calculated from the present model showed qualitatively good agreement with the experimental data.

In addition, Figs. 9 and 10b indicate a decreased sonic boom overpressure for both initial and tail overpressures in 59% of the

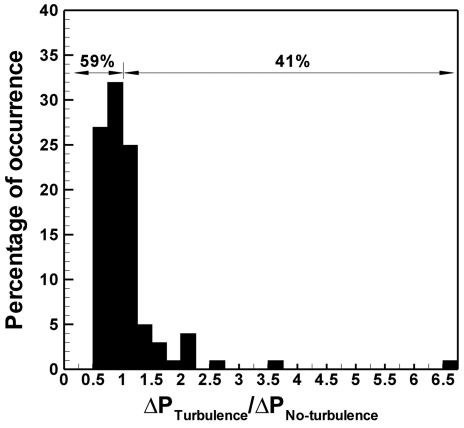

a) Initial overpressure

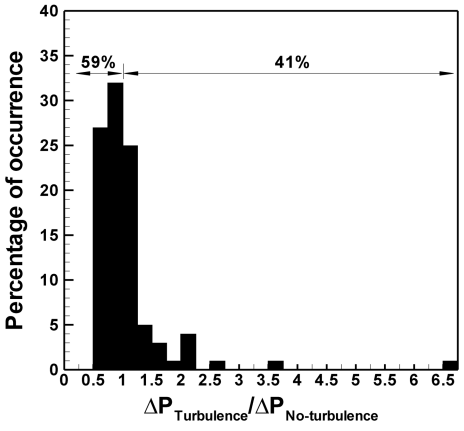

b) Tail overpressure

Fig. 9 Distribution of initial and tail overpressures for the 100 cases calculated with homogeneous atmospheric turbulence. The bin size was 0.25: a) initial overpressure and b) tail overpressure.

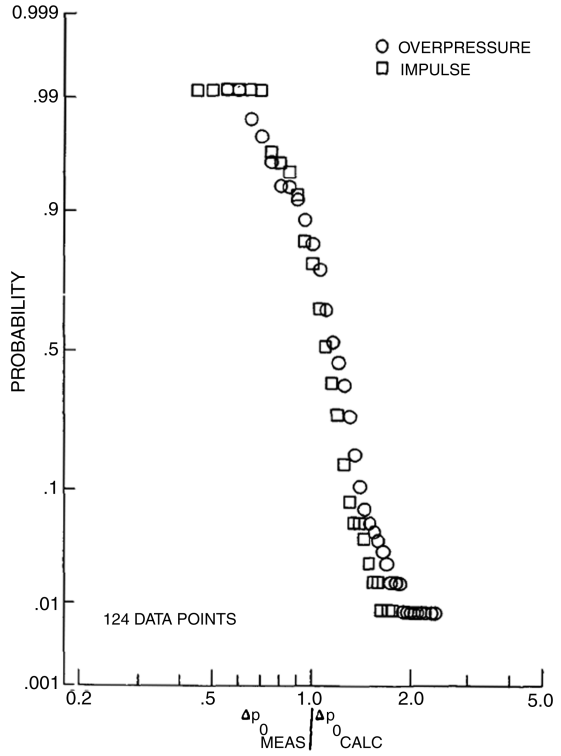

a) Experimental data for the XB-70 aircraft [11]

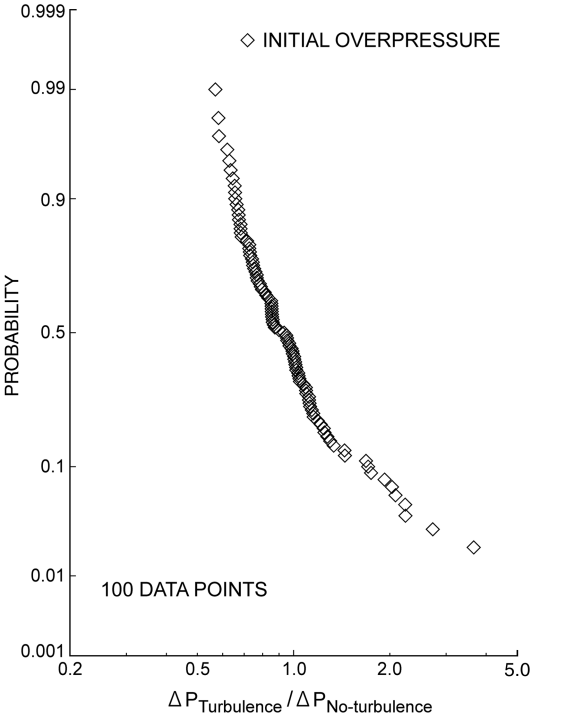

b) Calculated data from the present model

Fig. 10 Cumulative probability distributions for the overpressure: a) experimental data for the XB-70 aircraft obtained in June 1966 [11] and b) simulation data of initial overpressures for the 100 cases calculated with homogeneous atmospheric turbulence.

cases, whereas 41% of the cases had an increased overpressure as compared with the no-turbulence case. Therefore, it is likely that sonic boom overpressure will decrease due to homogeneous atmospheric turbulence. Similar results were obtained when calculating with 200 or 300 different turbulent fields.

As shown in Fig. 9, a few cases had extremely high overpressures, which were around 3.5 and 6.5 times the value for the no-turbulence case. However, it is reasonable to assume that such cases are unlikely to occur in the real world. First, Fig. 9 already shows that the probability of having these extreme values of overpressure is very low. In addition, the model used in this study was a simplified one, which considers only the velocity of the atmospheric turbulence; there are other factors that may affect sonic boom overpressure, such as temperature distribution in the atmosphere. The temperature distribution will alter the variability of sonic boom overpressure, as it affects local values of speed of sound and pressure in sonic boom calculations. Figure 9 also shows that the frequency distributions had the same shape for both the initial and tail overpressures, due to the strong correlation between initial and tail overpressures, as described in the discussion regarding Fig. 8b. Therefore, we now present a discussion of sonic boom overpressure, focusing on the results of the initial overpressure only.

To investigate the factors responsible for sonic boom variability, Fig. 11 shows the variation in the ray tube area with the altitude for the cases with a) increased and b) decreased sonic boom overpressure in comparison with the no-turbulence case. As shown in the figure, the variation in the ray tube area was generally not as smooth as in the no-turbulence case, for which this variation was approximately linear with altitude. Sonic boom overpressure is closely associated with the variation of ray tube area. Figures 11a and 11b show that the overpressure increased as the ray tube area on the ground decreased, and vice versa. These findings were consistent with the theoretical results from the geometrical acoustic approach, in which the wave amplitude is inversely proportional to the square root of the ray tube area.

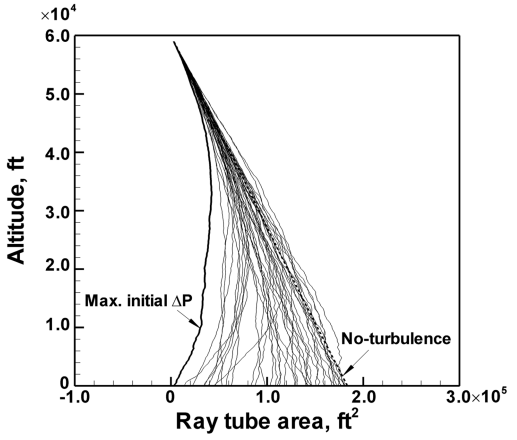

a) Case with increased boom overpressure

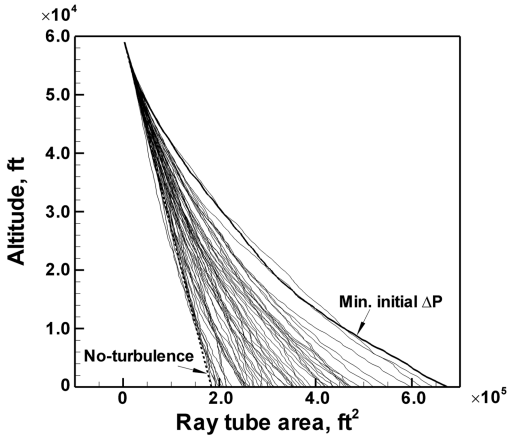

b) Case with decreased boom overpressure

Fig. 11 Variation of the ray tube area relative to altitude: cases with a) increased boom overpressure and b) decreased initial overpressure of sonic boom, as compared with the no-turbulence case.

C. Variability of Propagation Path and Arrival Point on the Ground

We assumed that the SST represented by the Sears–Haack body flew in the north–south direction, as shown in Fig. 4. Figure 12 shows a comparison of the propagation paths of sonic boom in the perpendicular plane for the following three cases: the first is the path calculated for the no-turbulence case, and the second and third are the northmost and southmost paths, respectively, among the 100 cases calculated with atmospheric turbulence. Figure 12 shows that the propagation paths for the previous three cases were approximately the same (i.e., homogeneous atmospheric turbulence had little, if any, appreciable effect on the propagation path). This is because the wind velocity of the homogeneous atmospheric turbulence was much smaller than the local speed of sound in the atmosphere. In fact, the rms velocity for the homogeneous atmospheric turbulence was set to $V_{\text{rms}} = 2.5\ \text{ms}^{-1}$, whereas the local speed of sound is around $a_0 = 300\ \text{ms}^{-1}$. Therefore, the local speed of sound controls the path of the sonic boom propagation.

On the other hand, Fig. 13 shows the distribution of the sonic boom ground arrival points for all cases, centered on the arrival point for the no-turbulence case. The horizontal axis is the north–south direction (direction of flight), and the vertical axis is the east–west direction

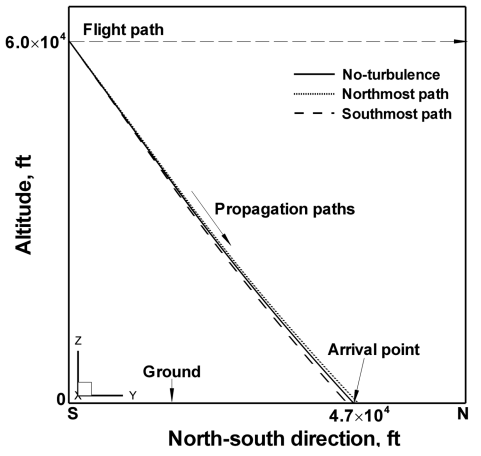

Fig. 12 Comparison of sonic boom propagation paths from the flight altitude to the ground for the following three cases: no-turbulence case, northmost path, and southmost path among all cases calculated with homogeneous atmospheric turbulence (flight was in the north–south direction).

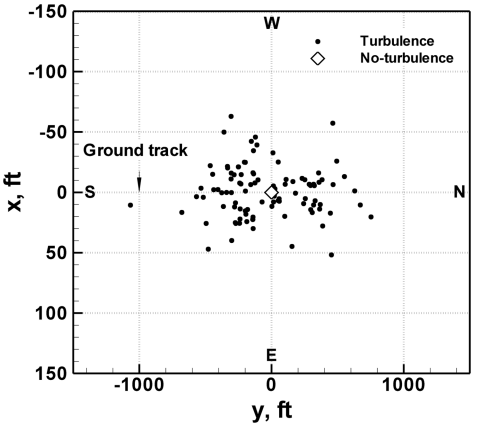

Fig. 13 Distribution of sonic boom arrival points on the ground for all cases. Flight was in the north–south direction, and the ground track (line $x = 0$) lay directly beneath the flight path at 60,000 ft.

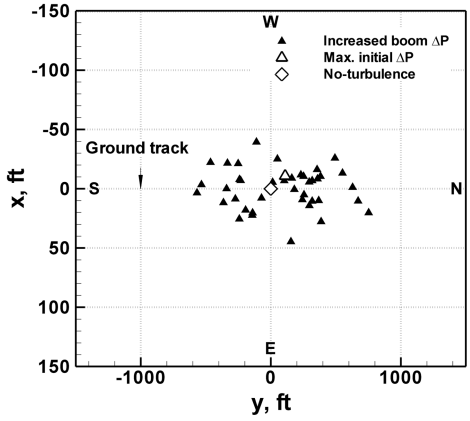

a) Case with increased boom overpressure

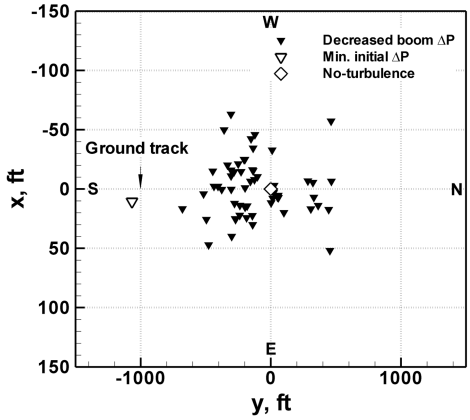

b) Case with decreased boom overpressure

Fig. 14 Distribution of sonic boom arrival points on the ground, including the no-turbulence case. These data suggest that there is no considerable correlation between the arrival point on the ground and the initial overpressure of sonic boom: cases with a) increased and b) decreased boom overpressure in comparison to the no-turbulence case.

(as shown in Fig. 4). The ground track (line $x = 0$) lay just beneath the flight path. As expected, the arrival point on the ground for the no-turbulence case occurred immediately over the ground track, whereas the arrival points for the turbulence cases were distributed randomly around the arrival point of the no-turbulence case. The arrival points on the ground were distributed over a range of approximately 1820 ft in the north–south direction and 115 ft in the east–west direction.

Finally, Fig. 14 shows the distribution of the arrival points on the ground for the cases with a) stronger and b) weaker initial overpressure in comparison to the no-turbulence case. Comparison of these figures revealed no clear correlation between boom overpressure and the location of the ground arrival point. Therefore, the increase or decrease in propagation distance from the flight altitude to the ground did not considerably affect sonic boom overpressure. This supports the observation that the variation of the ray tube area is the main cause of the variation in sonic boom overpressure, as mentioned in Sec. III.B.

IV. Conclusions

This study was performed to investigate the nondeterministic effects of homogeneous atmospheric turbulence on sonic boom propagation, focusing on the variability of sonic boom overpressure and propagation path geometry. Variations in sonic boom signatures are due to the variation in the ray tube area induced by homogeneous atmospheric turbulence. Specifically, we verified a decreased boom overpressure for increased ray tube areas, and the variability statistics of sonic boom overpressure obtained in the present model showed qualitatively good agreement with the experimental results for the XB-70 aircraft (June 1966). The present results indicated that 59% of the cases showed a decreased sonic boom overpressure in comparison to the no-turbulence case, whereas 41% of the cases showed an increased boom overpressure. Thus, homogeneous atmospheric turbulence seems to favor a decrease in sonic boom overpressure. In addition, homogeneous atmospheric turbulence had a fairly small influence on the propagation path, from the flight altitude to the ground. However, this influence still resulted in variability of the arrival point on the ground: 1820 ft in the north–south direction (direction of flight) and 115 ft in the east–west direction.

Acknowledgments

This study was supported by a grant from the research fellowships of the Japan Society for the Promotion of Science for Young Scientists. The authors wish to thank K. Kusunose of the Ministry of Defense and K. Matsushima of Tohoku University for their invaluable review of and comments on this work. The authors would like to express their gratitude to Y. Naka and Y. Makino of the Japan Aerospace Exploration Agency for their cooperation regarding the loudness calculation on the sonic boom signatures. The authors also wish to acknowledge our colleagues, especially F. K. Nakabayashi, for help in publishing this paper.

References

[1] Henne, P. A., "Case for Small Supersonic Civil Aircraft," *Journal of Aircraft*, Vol. 42, No. 3, 2005, pp. 765–774. doi:10.2514/1.5119

[2] Yoshida, K., and Makino, Y., "Aerodynamic Design of Unmanned and Scaled Supersonic Experimental Airplane in Japan," *Proceedings of the European Congress on Computational Methods in Applied Sciences and Engineering 2004* [CD-ROM], *Combination of CD-ROM Proceedings 951-39-1868-8 and 951-39-1869-6*, 2nd ed., 951-39-1868-8, 951-39-1869-6, Univ. of Jyvaskyla Dept. of Mathematical Info. Technology, Jyvaskyla, Finland, July 2004.

[3] Makino, Y., and Kroo, I., "Robust Objective Functions for Sonic-Boom Minimization," *Journal of Aircraft*, Vol. 43, No. 5, 2006, pp. 1301–1306. doi:10.2514/1.19442

[4] Kusunose, K., "A New Concept in the Development of Boomless Supersonic Transport," *Proceedings of the First International Conference on Flow Dynamics*, Tohoku Print, Sendai, Japan, Nov. 2004, pp. 46–47.

[5] Kusunose, K., Matsushima, K., Goto, Y., Yamashita, H., Yonezawa, M., Maruyama, D., and Nakano, T., "A Fundamental Study for the Development of Boomless Supersonic Transport Aircraft," AIAA Paper 2006-0654, Jan. 2006.

[6] Yamashita, H., Yonezawa, M., Obayashi, S., and Kusunose, K., "A Study of Busemann-Type Biplane for Avoiding Choked Flow," AIAA Paper 2007-0688, Jan. 2007.

[7] Yonezawa, M., Yamashita, H., Obayashi, S., and Kusunose, K., "Investigation of Supersonic Wing Shape Using Busemann Biplane Airfoil," AIAA Paper 2007-0686, Jan. 2007.

[8] Maruyama, D., Matsushima, K., Kusunose, K., and Nakahashi, K., "Aerodynamic Design of Biplane Airfoils for Low Wave Drag Supersonic Flight," AIAA Paper 2006-3323, June 2006.

[9] Kuratani, N., Ogawa, T., Yamashita, H., Yonezawa, M., and Obayashi, S., "Experimental and Computational Fluid Dynamics Around Supersonic Biplane for Sonic-Boom Reduction," AIAA Paper 2007-3674, May 2007.

[10] Plotkin, K. J., and George, A. R., "Propagation of Weak Shock Waves through Turbulence," *Journal of Fluid Mechanics*, Vol. 54, No. 3, 1972, pp. 449–467. doi:10.1017/S0022112072000795

[11] Maglieri, D. J., "Sonic Boom Flight Research: Some Effects of Airplane Operations and the Atmosphere on Sonic Boom Signatures," NASA SP-147, Apr. 1967.

[12] Kane, E. J., "Some Effects of the Atmosphere on Sonic Boom," NASA SP-147, Apr. 1967.

[13] Thomas, C. L., "Extrapolation of Sonic Boom Pressure Signatures by the Waveform Parameter Method," NASA TN D-6832, June 1972.

[14] Thomas, C. L., "Extrapolation of Wind-Tunnel Sonic Boom Signatures Without Use of a Whitham F-Function," NASA SP-255, Oct. 1970.

[15] Lipkens, B., and Blackstock, D. T., "Model Experiment to Study Sonic Boom Propagation through Turbulence Part 1: General Results," *Journal of the Acoustical Society of America*, Vol. 103, No. 1, Jan. 1998, pp. 148–158. doi:10.1121/1.421114

[16] Blanc-Benon, P., Lipkens, B., Dallois, L., Hamilton, M. F., and Blackstock, D. H., "Propagation of Finite Amplitude Sound through Turbulence: Modeling with Geometrical Acoustics and the Parabolic Approximation," *Journal of the Acoustical Society of America*, Vol. 111, Nos. 1–2, Jan. 2002, pp. 487–498. doi:10.1121/1.1404378

[17] Chernyshev, S. L., Kiselev, A. P., and Vorotnikov, P. P., "Sonic Boom Minimization and Atmospheric Effects," AIAA Paper 2008-0058, Jan. 2008.

[18] Takaki, R., Yamamoto, K., Yamane, T., Enomoto, S., and Mukai, J., "The Development of the UPACS CFD Environment," *Lecture Notes in Computer Science*, Vol. 2858, Springer, Berlin, 2003, pp. 307–319.

[19] Sears, W., "On Projectiles of Minimum Wave Drag," *Quarterly of Applied Mathematics*, Vol. 4, No. 4, Jan. 1947, pp. 361-366.

[20] Raymer, D. P., *Aircraft Design: A Conceptual Approach*, 4th ed., AIAA, Reston, VA, 2006, pp. 338–341.

[21] Liepmann, H. W., and Roshko, A., *Elements of Gasdynamics*, Wiley, New York, 1957, pp. 107–123, 389.

[22] Hinze, J., *Turbulence*, 2nd ed., McGraw–Hill, New York, 1975, Chap. 3, pp. 175–320.

[23] Orlanski, I., "A Rational Subdivision of Scales for Atmospheric Processes," *Bulletin of the American Meteorological Society*, Vol. 56, No. 5, 1975, pp. 527–530.

[24] Bechara, W., Bailly, C., Lafon, P., and Candel, S. M., "Stochastic Approach to Noise Modeling for Free Turbulent Flows," *AIAA Journal*, Vol. 32, No. 3, 1994, pp. 455–463. doi:10.2514/3.12008

[25] Endlich, R. M., Singleton, R. C., and Kaufman, J. W., "Spectral Analysis of Detailed Vertical Wind Speed Profiles," *Journal of the Atmospheric Sciences*, Vol. 26, No. 5, 1969, pp. 1030–1041. doi:10.1175/1520-0469(1969)026<1030:SAODVW>2.0.CO;2

[26] Chkhetiani, O. G., Eidelman, A., and Golbraikh, E., "Large- and Small-Scale Turbulent Spectra in MHD and Atmospheric Flows," *Nonlinear Processes in Geophysics*, Vol. 13, No. 6, 2006, pp. 613–620.

[27] Heilman, W. E., and Bian, X., "Combining Turbulent Kinetic Energy and Haines Index Predictions for Fire-Weather Assessments," *Proceedings of the 2nd Fire Behavior and Fuels Conference: The Fire Environment-Innovations, Management, and Policy*, RMRS-P-46CD, U.S. Forest Service, Washington, D.C., Mar. 2007, pp. 159–172.

[28] Risso, F., Corjon, A., and Stoessel, A., "Direct Numerical Simulations of Wake Vortices in Intense Homogeneous Turbulence," *AIAA Journal*, Vol. 35, No. 6, 1997, pp. 1030–1040. doi:10.2514/2.191

[29] Hayes, W. D., and Runyan, H. L., Jr., "Sonic-Boom Propagation Through a Stratified Atmosphere," *Journal of the Acoustical Society of America*, Vol. 51, Nos. 2–3, Nov. 1972, pp. 695–701. doi:10.1121/1.1912903

[30] Anderson, J. D., Jr., *Introduction to Flight*, 4th ed., McGraw–Hill, New York, 2000, pp. 94–99, 709–720.

[31] Makino, Y., Aoyama, T., Iwamiya, T., Watanuki, T., and Kubota, H., "Numerical Optimization of Fuselage Geometry to Modify Sonic-Boom Signature," *Journal of Aircraft*, Vol. 36, No. 4, 1999, pp. 668–674. doi:10.2514/2.2509

[32] Darden, C. M., Olson, E. D., and Shields, E. W., "Elements of NASA High-Speed Research Program," AIAA Paper 93-2942, July 1993.

[33] Maglieri, D. J., Huckel, V., Henderson, H. R., and Putman, T., "Preliminary Results of XB-70 Sonic Boom Field Tests During National Sonic Boom Evaluation Program," NASA LWP 382, Mar. 1967.

[34] Hubbard, H. H., Maglieri, D. J., and Huckel, V., "Variability of Sonic Boom Signatures With Emphasis on the Extremities of the Ground Exposure Patterns," NASA SP-255, Oct. 1970.